Visualization Study of Flow Condensation in Hydrophobic Microchannels

Yongping Chen
School of Hydraulic, Energy and Power Engineering, Yangzhou University, Yangzhou, Jiangsu 225127, P.R. China

Key Laboratory of Energy Thermal Conversion and Control of Ministry of Education, School of Energy and Environment, Southeast University, Nanjing, Jiangsu 210096, P.R. China

Chaoqun Shen, and Mingheng Shi
Key Laboratory of Energy Thermal Conversion and Control of Ministry of Education, School of Energy and Environment, Southeast University, Nanjing, Jiangsu 210096, P.R. China

George P. Peterson
George W. Woodruff School of Mechanical Engineering, Georgia Institute of Technology, Atlanta, GA 30332

DOI 10.1002/aic.14319

A visualization study on flow condensation in hydrophobic rectangular silicon microchannels with hydraulic diameter of approximately 150 μm is conducted. Thin Au film with thickness of 200 nm is sputtered on channel surfaces to create a hydrophobic surface with an equilibrium contact angle of approximately 96°. In addition to traditional droplet flow, droplet-annular compound flow, droplet-injection compound flow, and droplet-bubble/slug compound flow are also observed. The results indicate that injection location is postponed, and injection frequency increases with increasing inlet vapor Reynolds number and condensate Weber number. An empirical correlation of the injection location and injection frequency are presented and discussed. In particular, for a larger inlet vapor Reynolds number, the injection flow is closer to the channel outlet and the condensation heat transfer is enhanced. © 2014 American Institute of Chemical Engineers *AIChE J*, 60: 1182–1192, 2014

Keywords: condensation, hydrophobic microchannels, flow pattern, heat transfer

Introduction

Because of potential impact of MEMS thermal devices, such as micro heat pipes, chip-based laboratories, micro fuel cells, microreactors, micro thermal control systems, and formation of single-walled carbon-nanotube networks,[1–3] flow condensation in microchannels has received considerable attention. Many early experimental results indicate that the flow condensation in microchannels is quite different from that occurs in larger channels.[4–6] So far as the gas–liquid two-phase flow in confined microspace, the surface tension becomes the dominating force and effectively replaces normal body forces found in conventional macrochannels.[1,4]

Transition of condensation flow patterns is an important index of condensation heat transfer. Médéric et al.[4] performed a visualization study on condensation flow patterns in tubes with diameters of 0.56, 1.1, and 10 mm and found that capillary force is the dominating factor in channels with diameters less than 1 mm. Coleman and Garimella,[6] Agarwal et al.,[7,8] and Bandhauer et al.[9] studied condensation of Refrigerant R134a in circular microchannels with hydraulic diameters ranging from 0.506 to 1.524 mm and noncircular microchannels with hydraulic diameters ranging from 0.1 to 0.839 mm for different mass fluxes.

Chen et al.[10–12] conducted several experiments on the condensation of steam in triangular, trapezoidal, and rectangular microchannels, with characteristic dimensions in the range of dozens micrometers. Of particular interest is the observation of injection flow, which has been identified as the eigen pattern of microscale flow condensation. In addition, Wu et al.[13,14] and Quan et al.[15–17] also studied the influence of condition parameters on injection flow, condensation pressure drop, and heat transfer during flow condensation in trapezoidal microchannels. Ma et al.[18] investigated the influence of cross-sectional geometry on the steam flow condensation in trapezoidal microchannels, indicating that the nonuniform surface tension at liquid–vapor interface causes Marangoni convection. Subsequently, they evaluated the effect of surface free energy on flow condensation.[19] Zhang et al.[20,21] studied the bubble emissions in microchannels with a hydraulic diameter of 58 μm and observed different bubble sizes and bubble detachment frequencies for different cooling rates.

By comparing the condensation behaviors in microchannels with different cross-sectional shapes, Kuo and Pan[22]

Correspondence concerning this article should be addressed to Y. Chen at chenyp@yzu.edu.cn.

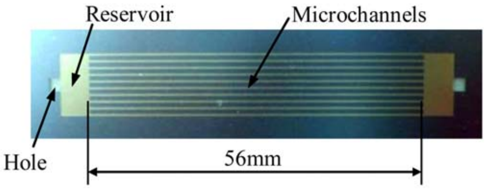

(a) Photo of experiment chip

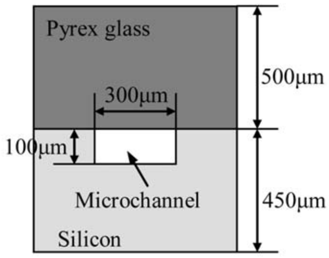

(b) Cross-section of microchannel

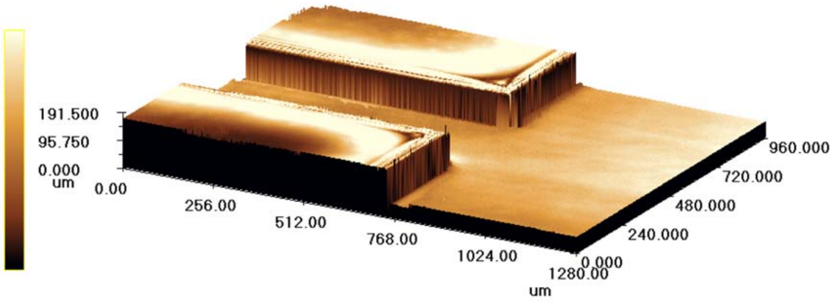

(c) Micrograph of the microchannel

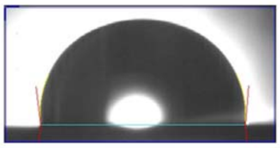

(d) Contact angle

Figure 1. Schematic of the silicon microchannels chip.

[Color figure can be viewed in the online issue, which is available at wileyonlinelibrary.com.]

found that, for condensation in the mist/annular flow regimes, microchannels with uniform cross-sections had higher heat transfer coefficients than those with converging cross-sections. Fang et al.[23] reconstructed three-dimensional liquid film profiles based on measurements using optical interferometery and studied the influence of the film thickness on condensation in hydrophilic microchannels. Fang et al.[23] also observed three different flow transition modes in microchannels with different aspect ratios.

It is well documented that the flow condensation is significantly influenced by surface wettability. In general, a hydrophobic surface has a contact angle larger than 90° on which a droplet can grow. For droplet condensation, the steam helps to maintain contact with coolant surface. In this case, heat released from the steam transfers to coolant surface directly without thermal resistance of the condensate film. Therefore, when compared with film condensation, droplet condensation has the potential to deliver an order of magnitude increase in the heat transfer capability. It is clear that by combining twos of these enhancements, microscale and droplet, a greater overall enhancement in the condensation heat transfer could be realized.

Many early investigations have been carried out on droplet condensation on hydrophobic surfaces.[24–29] In open space, surface wettability and surface microstructure influence condensation behaviors. However, the available study on condensation in a confined hydrophobic space, especially in microchannels, is very limited. Fang et al.[30] experimentally investigated the steam condensation in silicon microchannels with three different wall hydrophobicities. The heat transfer rates and pressure drops were measured in hydrophobic microchannels and compared with hydrophilic channels. The investigation indicates that, due to the slug instabilities, flow pattern transition from dropwise/slugwise flow to plug flow is observed in hydrophobic channels. However, in this investigation, flow characteristics were not quantified or analyzed.

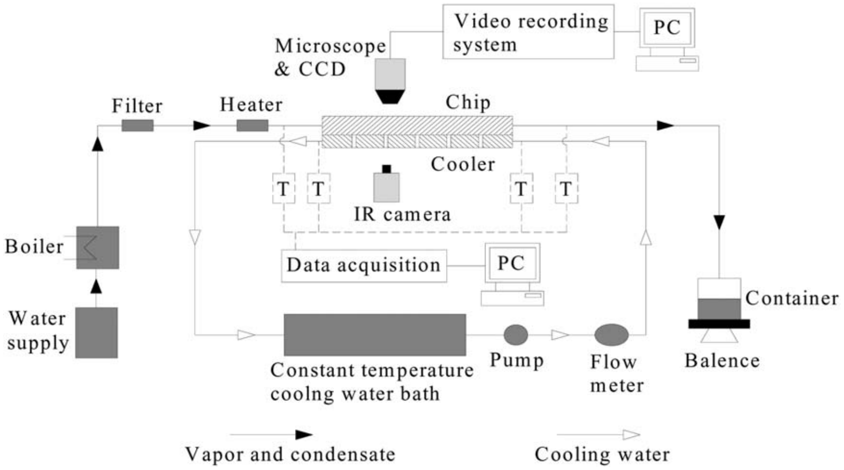

Figure 2. Schematic of experimental setup of condensation in hydrophobic microchannels.

To provide a more detailed understanding of the underlying physics of hydrophobicity on microcondensation, a visualization study for steam condensation in hydrophobic rectangular microchannels with hydraulic diameters of 150 μm and a liquid equilibrium contact angle of 96° is conducted to capture the condensation flow patterns. In addition, the injection parameters and heat transfer characteristics of flow condensation in hydrophobic rectangular microchannels are investigated and discussed.

Experimental Descriptions

Fabrication of microchannels

The samples fabricated in the current investigation, having 10 parallel rectangular microchannels with an effective length, L, of 56 mm, a hydraulic diameter of 150 μm and aspect ratio of 3, is etched on <100> silicon wafers through deep reactive ion etching. The center distance between the two adjacent channels is 1 mm. To seal the channel, a Pyrex glass is anodically bonded on the top of the wafer. Figure 1 illustrates a schematic of the chip. A thin Au film with a thickness of 200 nm is sputtered on the silicon wafer surface to create a hydrophobic surface. Equilibrium contact angle of the treated silicon wafer surface is 96°, as shown in Figure 1(d). Static sessile drop method[31] is applied to measure the contact angle. It should be noted that the Pyrex glass surface (i.e., the upper part of the microchannel) is not treated and is hydrophilic.[32]

Cheng and Wu[33] recommended to classify the micro-, meso- (or mini-), and marcochannels in terms of the bond number, Bo, which is defined as

$$Bo=\frac{g(\rho_l-\rho_v)D_h{}^2}{\sigma} \tag{1}$$

where g, ρ_l, ρ_v, D_h, and σ are gravity, liquid density, vapor density, hydraulic diameter of microchannel, and surface tension, respectively. Based on the theoretic analysis of Li and Wang,[34] the channel can be regarded as a microchannel if $Bo < 0.05$, where the gravity effect can be neglected. In our experiment, the used channels are microchannels as Bo is approximately 0.004.

Table 1. Uncertainties of Parameters

Parameters	Maximum Uncertainties (%)	Parameters	Maximum Uncertainties (%)
X_p/L	2.21	h	8.51
f_p	3.04	Re_v	4.86
Q	8.24	We_l	6.78

Experimental setup

The experimental setup is illustrated in Figure 2. The saturated steam, generated by the boiler, flows through the filter and then arrives at the microchannels in which vapor condenses and releases heat to cooling water in the cooler. To reduce the thermal resistance, high-temperature thermally conductive grease is coated on contact surface between chip and cooler. The entire experimental section, with the exception of the place for photography, is covered by thermal insulation materials to reduce the heat loss.

In the current investigation, T type thermocouples (accuracy: ±0.1 K) are used to measure the temperature at inlet and outlet of both microchannel and cooler. Due to the uncertainty in measurements of channel surface temperature via thermocouples, the surface temperature is measured through a noncontact measurement method. The infrared radiation (IR) imaging (NEC TH9260 Thermo Tracer, accuracy: ±2%) is used to measure the temperature of silicon channel surface. The channel wall temperature measured by IR has been verified using single phase flowing in chip without cooler. There are five IR probe holes (diameter 1 mm) are manufactured on the cooler for the tracer to identify the chip wall temperature. The volume flow rate of the cooling water is measured and adjusted via a glass rotor flow meter (accuracy: ±0.1 mL/s). The condensate is collected by the container on an electronic balance (accuracy: ±0.01 g). Weighing the condensate at the outlet is utilized to measure the steam mass flow rate in the experiment. Another approach, measuring the condensation heat transfer based on the thermal balance, is applied to verify the steam mass flow rate. For these two approaches, the deviation of steam mass flow rate is found to range between 0.7 and 17.6% and with an average of 9.5%. The flow patterns are recorded using a microscope (Zoom 160 optical system) and a high-speed video camera (Photron SA4). Different experiment conditions are acquired by regulating inlet saturated steam pressure and flow rate of the cooling water.

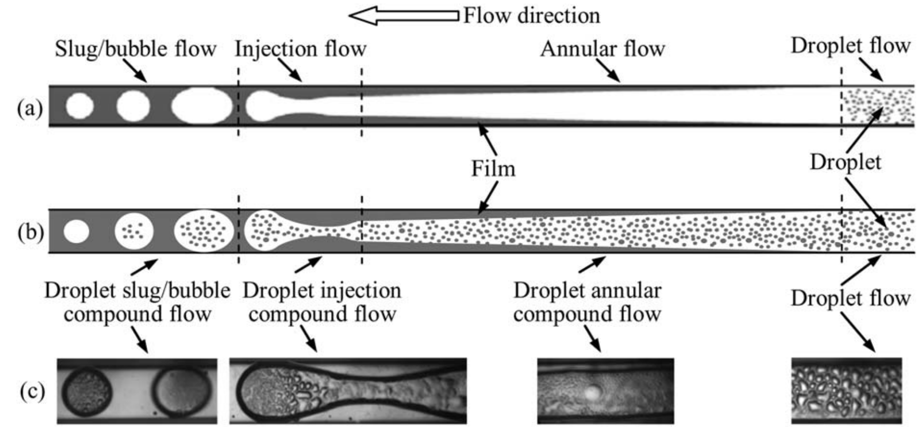

(a) Schematic diagram of flow patterns in microchannels without treatment [11]

(b) Schematic diagram of flow patterns in microchannels in our current work

(c) Observed images correspond to different flow patterns in our current work

Figure 3. Schematic of flow patterns in microchannels with and without treatment.

Data analysis

The frequency of the injection flow is acquired from the image number for injection flow period recorded by video recording system. If f is the exposure frequency and M is the number of injection periods recorded by N photographs, the injection frequency f_p can be calculated as

$$f_p = \frac{fM}{N} \tag{2}$$

The average heat transfer coefficient is

$$h = \frac{q}{(t_f - t_w)} \tag{3}$$

where q is the average heat flux, t_f is the average temperature of condensation flow, t_w is the average temperature of channel wall. The average heat flux in whole channel is

$$q = \frac{Q}{nA} \tag{4}$$

in which n and A are channel number and heat transfer area, respectively, including two-sided areas and the bottom area

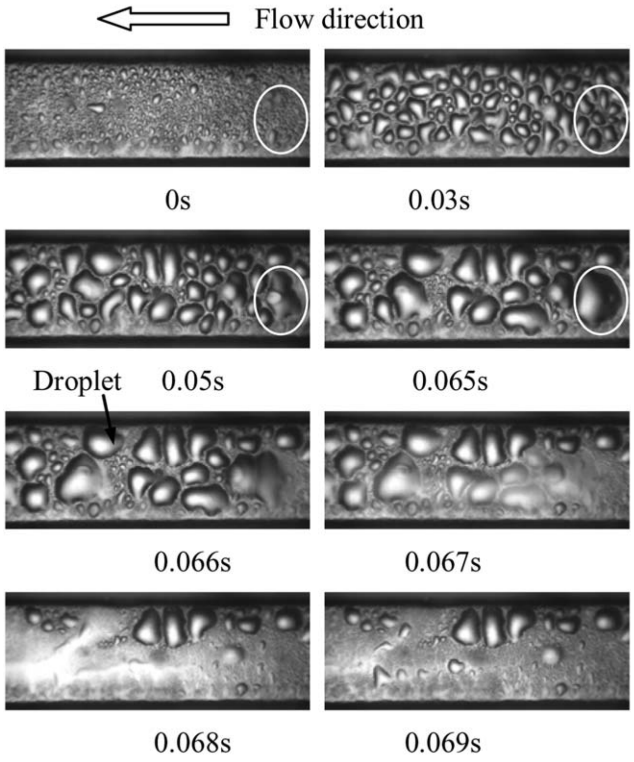

Figure 4. Droplet flow ($Re_v = 456$, $Q = 26.8$ W, $X/L = 0.04$).

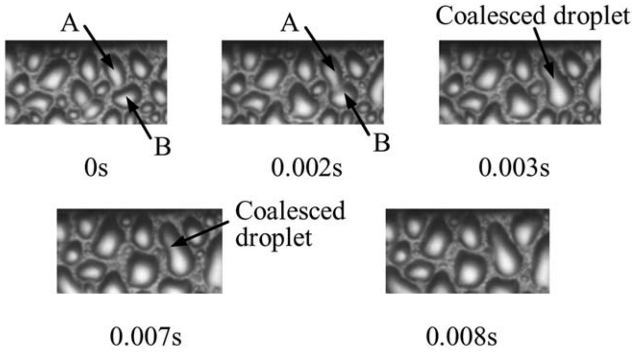

Figure 5. Coalescence of two droplets.

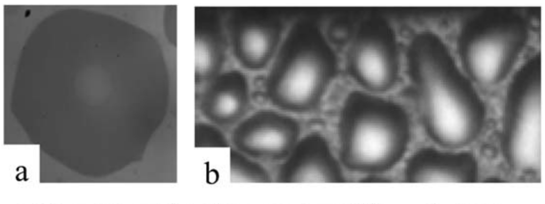

a. Droplet on the glass captured through glass

b. Droplets on the silicon surface in channels

Figure 6. Comparison of droplet on glass and silicon surface.

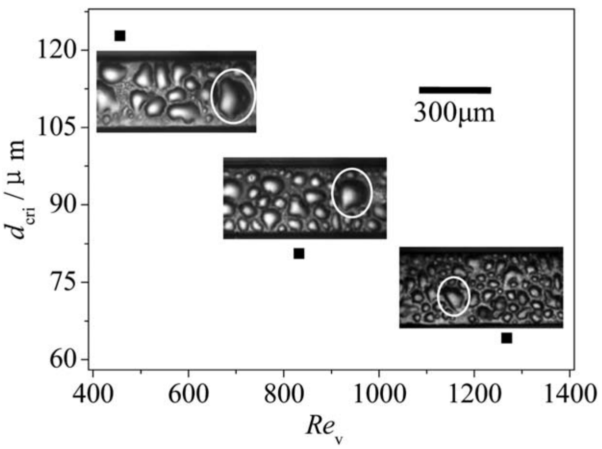

Figure 7. Critical size for droplet detaching from the wall versus $\mathrm{Re_v}$.

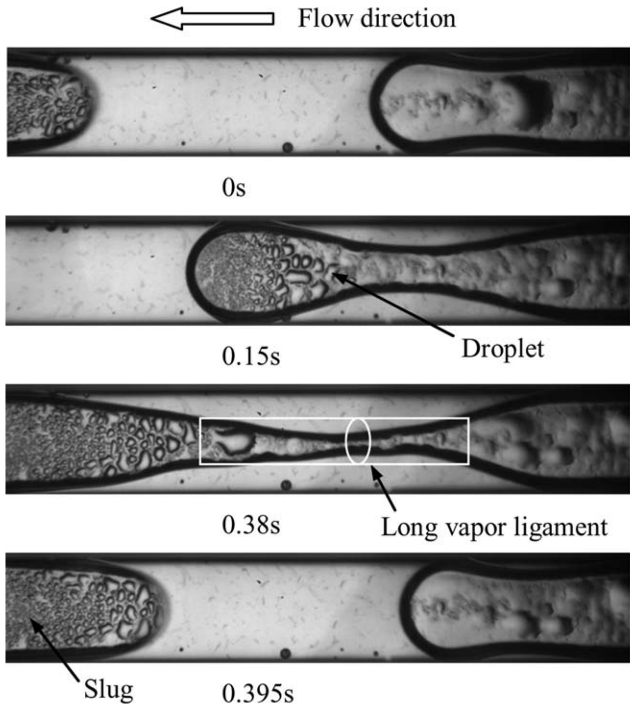

Figure 9. Droplet-injection compound flow (Condition 1) ($\mathrm{Re_v} = 471$, $Q = 29.2$ W, $X_p/L = 0.16$).

in one single-channel (with the adiabatic glass top area exclude). The heat flow rate Q can be calculated by

$$Q=c_{\mathrm{p}}\rho_{\mathrm{cw}}G_{\mathrm{cw}}\left(t_{\mathrm{cw,out}}-t_{\mathrm{cw,in}}\right) \tag{5}$$

where $t_{\mathrm{cw,out}}$, $t_{\mathrm{cw,in}}$, G_{cw}, c_{p}, and ρ_{cw} are outlet temperature, inlet temperature, volume flow rate, specific heat, and density of the cooling water, respectively.

Based on the pressure drop model of two-phase water-steam,[35] in this work, the pressure drop upstream the injection flow point is estimated to be in the range between 0.2 and 2.1 kPa. The measured overall pressure drop between the chip inlet and outlet ranges between 32.9 and 132.9 kPa. In the comparison, it can be seen that the pressure drop of two-phase water-steam flow in the upstream "steam" portion is much smaller than the measured overall pressure drop between the chip inlet and outlet. On this basis, condensing temperature before the injection point is assumed to be the inlet steam temperature. And linear distribution of condensing temperature is assumed to be after the injection point. Therefore, the average condensing temperature, t_{f}, can be computed by

$$t_{\mathrm{f}}=\frac{t_{\mathrm{f,up}}X_{\mathrm{p}}+t_{\mathrm{f,down}}\left(L-X_{\mathrm{p}}\right)}{L}=\frac{t_{\mathrm{in}}+t_{\mathrm{out}}}{2}+\frac{X_{\mathrm{p}}}{L}\frac{t_{\mathrm{in}}-t_{\mathrm{out}}}{2} \tag{6}$$

where $t_{\mathrm{f,up}}$ is the average temperature upstream the injection flow and assumed to be equal to inlet saturated steam temperature (t_{in}). $t_{\mathrm{f,down}}$ is the average temperature downstream the injection flow and approximately equal to the average of the saturated steam temperature (t_{in}) and the outlet condensation temperature (t_{out}). The average temperature of the channel wall, t_{w}, is the algebraic average of measured temperature on wall surface.

The inlet vapor Reynolds number $\mathrm{Re_v}$ and condensation Weber number $\mathrm{We_l}$ are derived by

$$\mathrm{Re}_{\mathrm{v}}=\frac{m_{\mathrm{l}}D}{n\upsilon_{\mathrm{v}}\rho_{\mathrm{v}}A_{\mathrm{c}}} \tag{7}$$

$$\mathrm{We}_{\mathrm{l}}=\frac{\rho_{\mathrm{l}}D}{\sigma}\left(\frac{m_{\mathrm{l}}}{n\rho_{\mathrm{l}}A_{\mathrm{c}}}\right)^{2} \tag{8}$$

where m_{l} is the condensation flow rate, D is the hydraulic diameter of channel, υ_{v} and σ are the saturated vapor viscosity and surface tension, respectively, ρ_{v} and ρ_{l} are saturated vapor density and condensate, and A_{c} is cross-sectional area of channel.

In about 5 min, chip surface temperature, inlet and outlet temperature of channel and cooler as well as mass flow

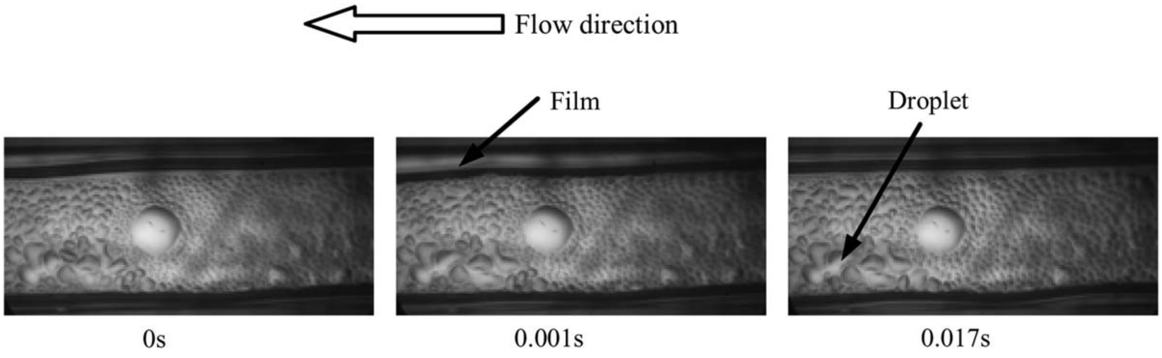

Figure 8. Droplet-annular compound flow ($\mathrm{Re_v} = 906$, $Q = 54.2$ W, $X/L = 0.94$).

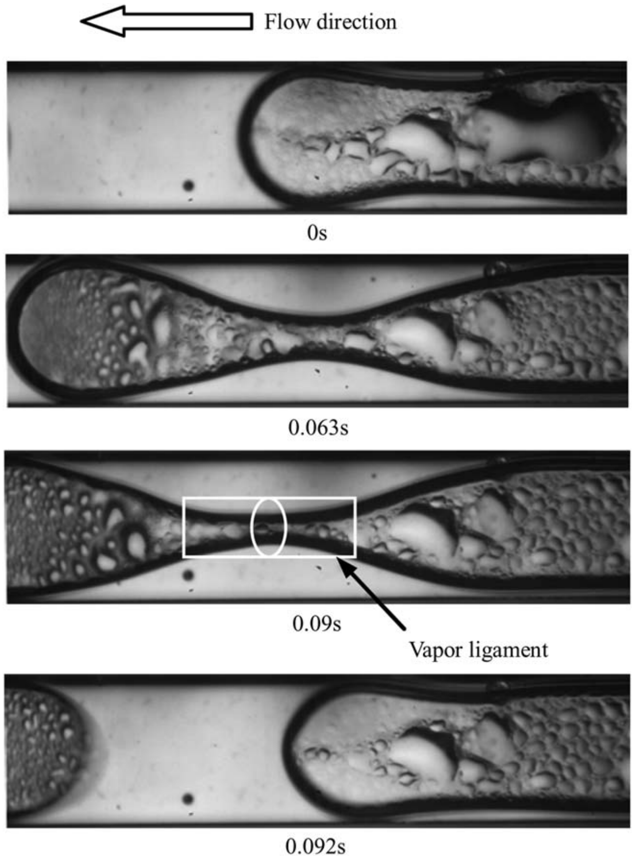

Figure 10. Droplet-injection compound flow (Condition 2) ($Re_v = 637$, $Q = 39.7$ W, $X_p/L = 0.43$).

rate of vapor and cooling water are recorded in every 10 s under steady state for one experimental case. Experimental cases with the inlet vapor Reynolds numbers ranging from 408 to 1042 are taken into account in this study. And the average values of these measurements are taken for the experimental results. Due to the high thermal conductivity of silicon and thin silicon wafer, the thermal resistance of silicon wafer is very small, that is, the temperature difference between channel surface and silicon wafer outer surface can be considered negligible. In the experiment, the channel wall temperature is measured on the backside of silicon channel. The heat loss mainly includes the released heat through outer surface of experimental section (i.e., insulation layer of cooler and chip) in a fashion of natural convection.

Based on the data error analysis, the uncertainties of various parameters in this article are listed in Table 1.

Experimental Results and Discussion

Flow pattern visualization

In nontreated silicon microchanel, the droplet, annular, injection, and slug-bubbly flow are the dominant flow patterns along the silicon microchannels, as shown in Figure 3(a). Differing from conventional silicon microchannels, droplet flow is always accompanied in the whole condensation process for hydrophobic microchannel. The droplet-slug/bubble compound flow, droplet-injection compound flow, droplet-annular compound flow, and droplet flow are observed in our current work, as described in Figures 3(b) and (c).

Droplet flow is observed at the channel inlet. Figure 4 (0–0.065 s) shows the growth and coalescence process of droplets. As shown in the figure, droplets coalesce while contacting with each other and the coalesced droplet is bigger than the previous ones. Then, droplets detach and slid on the channel surface after reaching a critical size. Synchronously, detached droplets sweep other droplets on their way downstream (as shown in Figure 4 [0.066–0.068 s]). A more detailed coalescence process of droplets is presented in Figure 5. Droplet A and Droplet B coalesce into one, and then the coalesced big droplet coalesces with another small droplet as shown in Figure 5 (0.007 s).

Although the flow pattern can only be observed from the chip top to obtain 2D image, we can roughly and qualitatively justify the effect of depth dimension through the distinction of droplet size and brightness. The droplet height is mainly dependent on the droplet size and the contact angle. Due to reflected light, the droplet top in 2D image is brighter than the droplet edge. According to droplet size, the droplet height as shown in 0.003 s of Figure 5 is larger than that in 0 s of Figure 5, which means that the droplet grows along with the condensation process.

Thermal conductivity of silicon [105 W/(m K)[36]] is much larger than that of Pyrex glass [1.25 W/(m K)[37]], and the upper Pyrex glass is covered by thermal insulation material except the view region for capturing flow patterns during the experiment. The upper side of Pyrex glass can be regarded

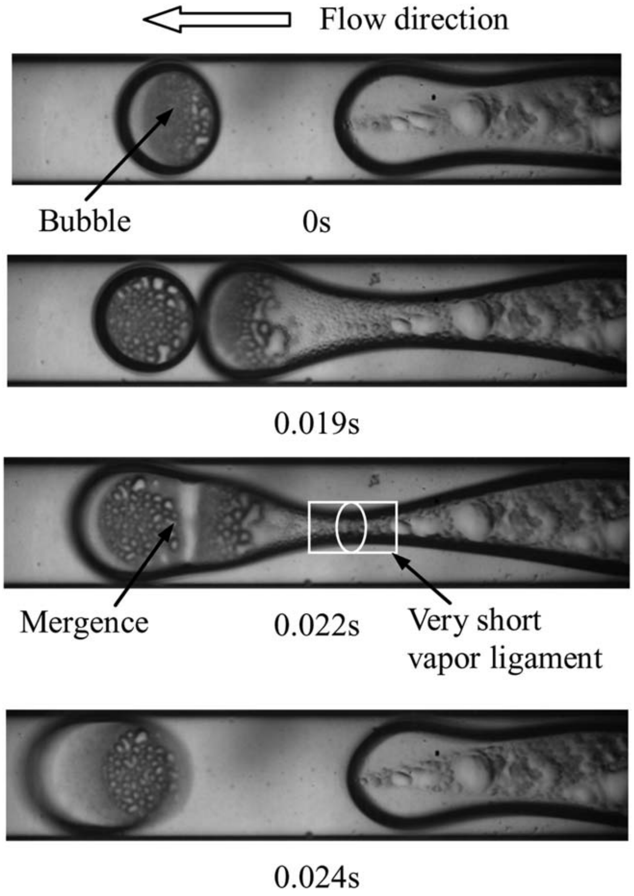

Figure 11. Droplet-injection compound flow (Condition 3) ($Re_v = 1004$, $Q = 60.4$ W, $X_p/L = 0.91$).

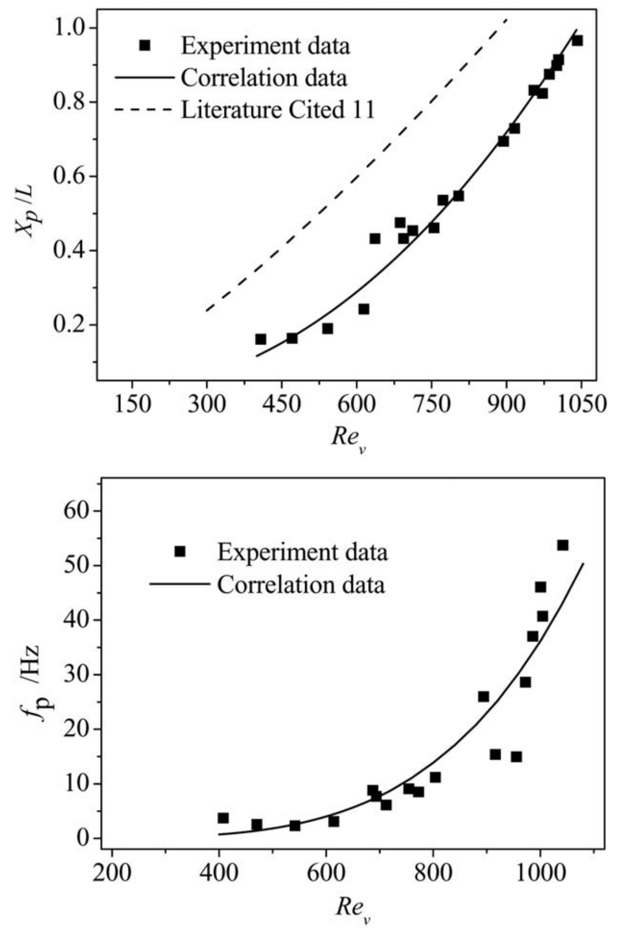

Figure 12. Injection location and frequency versus Re_v.

as adiabatic. Therefore, in the experiment, almost all the heat releases to the cooler through silicon wafer and no vapor condense on the Pyrex glass. To confirm such a point, we conduct an experiment to compare droplet images (Figure 6) observed on the Pyrex glass and silicon wafer. As seen from the figure, if Pyrex glass is covered with droplet, the brightness of droplet on glass surface is weaker than that in microchannel chip. Therefore, the droplets obtained in this work are located on the bottom silicon wafer but not on the upper Pyrex glass. The effect of Pyrex glass on the condensation can be considered as negligible in the experiment.

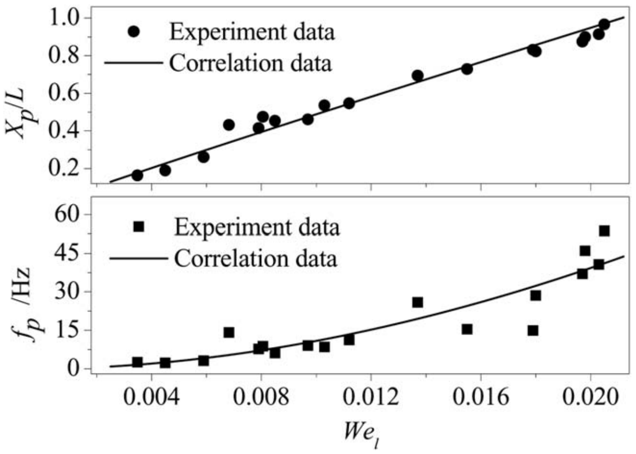

Figure 13. Injection location and frequency versus We_l.

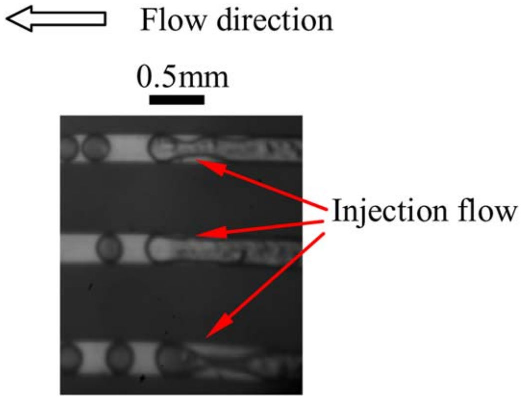

Figure 14. Injection point distribution among parallel channels.

[Color figure can be viewed in the online issue, which is available at wileyonlinelibrary.com.]

If the drag force [38–40] acting on the droplet overcomes the retentive force,[41] the droplet on the hydrophobic surface slides along the flow direction. Thus, once the droplet coalesces and increases to a critical size (the maximum droplet diameter when detachment occurs), the steam drag force on the droplet is large enough to overcome the force holding the droplet on the solid surface and then the coalesced droplet detaches. To provide a further insight into the condensate droplet at hydrophobic surface in steam flow, Figure 7 presents the dependence of critical diameter on the inlet vapor Reynolds number. In the inset, the droplets enclosed by ellipses tend to detach from the wall. As expected, the critical size of droplet diameter when detachment occurs decreases with inlet vapor Reynolds number.

As channel height is much smaller than channel width, the condensate may entirely cover the short sidewalls (height) while droplet still exists on the wide sidewall (width) surface. In this work, as shown in Figure 8, droplet-annular compound flow is observed in the hydrophobic microchannels. The capture point of Figure 8 is about 1 mm upstream of the injection flow.

Due to the hydrophobic surface, a new flow pattern, droplet-injection compound flow is found at the end of the droplet-annular compound flow. In this type of injection flow, droplets still exist, which are quite different from that in silicon microchannels without surface treatment.[10–12] Figures 9–11 shows three vapor slug/bubble breakup modes of droplet-injection compound flow under different experimental conditions.

With a low inlet vapor Reynolds number of 471 at the heat flow rate of 29.16 W, there is a long vapor ligament (as shown in the rectangle in Figure 9 [0.38 s]) between vapor column and vapor slug. Droplets obviously exist in both the injection flow and the emitted vapor slug. With the increasing Re_v, vapor ligament gets shorter, as shown in Figure 10. Figure 11 illustrates vapor bubble breakup mode with very short vapor ligament at the condition of inlet vapor Reynolds number of 1004 and heat flow rate of 60.4 W. The vapor bubble, which does not completely divorce from the ligament, impacts the previous emitted bubble (Figure 11 [0.019–0.022 s]), and then they merge into one bigger slug and flow downstream rapidly.

Figure 12 presents the variation of dimensionless injection location, X_p/L, and injection frequency, f_p, versus the inlet

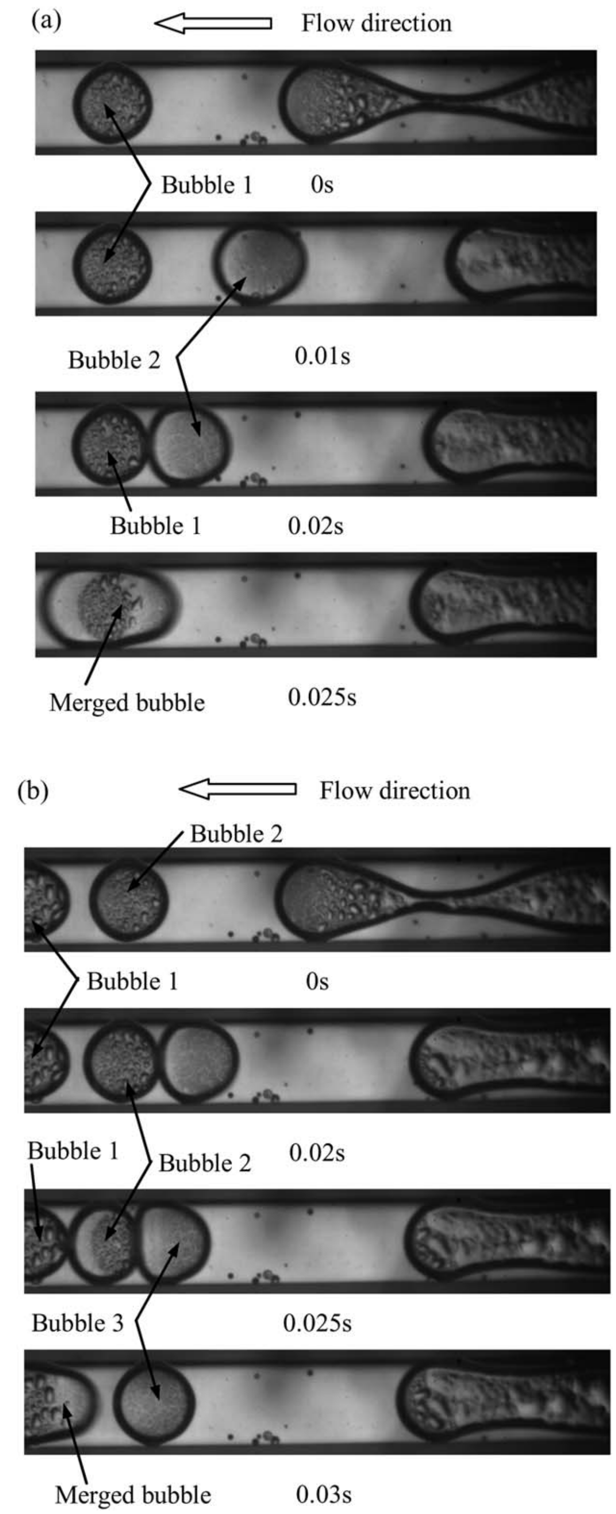

Figure 15. Droplet-slug/bubble compound flow ($Re_v = 687$, $Q = 42.6$ W, $X/L = 0.48$).

vapor Reynolds number, Re_v, in a hydrophobic microchannel. As shown in this figure, the location of injection flow increases with increasing Re_v and the injection frequency increases with the increase of inlet vapor Reynolds number, which is similar to the experiment data in wide rectangular[11] and triangular[12] silicon microchannels without surface treatment. However, benefiting from the hydrophobicity, droplet condensation occupies more area on channel surface than that in conventional silicon microchannels, a higher condensation heat transfer coefficient is realized in hydrophobic microchannels and the vapor can be condensed in a shorter distance. Therefore, compared with the conventional wide rectangular silicon microchannels, the location of droplet-injection compound flow in hydrophobic microchannels is closer to the inlet at the same inlet vapor Reynolds number.

The surface tension is another important factor affecting the location and frequency of injection flow. Figure 13 presents relations of X_p/L and f_p with condensate Weber number, which indicates the ratio of inertia force and surface tension in the condensate. Both the X_p/L and f_p increase with the increasing We_l.

The location and frequency of injection flow are both related to the inlet vapor Reynolds number and the condensate Weber number. Therefore, based on experimental data, the correlations of X_p/L and f_p are presented, respectively, as

$$X_p/L = 0.257\times10^{-2}\ Re_v^{1.124}\ We_l^{0.479},\ 408 \le Re_v \le 1042,\ 0.0025 \le We_l \le 0.0212 \quad (9)$$

$$f_p = 0.483\times10^{-3}\ Re_v^{2.153}\ We_l^{0.923},\ 408 \le Re_v \le 1042,\ 0.0025 \le We_l \le 0.0212 \quad (10)$$

Correlation values of injection dimensionless location, X_p/L, and frequency, f_p, are compared with the experimental data. The average deviations of Eqs. (9) and (10) from the experimental data are 8.2 and 20.6%, respectively.

Despite that droplet-injection compound flow is an unstable characteristic flow pattern in hydrophobic microchannels, the location and the frequency of this flow are unaltered when the experimental condition is not changed. In addition, it is observed that the injection point is almost at the same location among the parallel channels, as shown in Figure 14.

Droplet-slug/bubble compound flow is observed after the droplet-injection compound flow. As shown in Figure 15, after injection, the emitted bubbles merge to form vapor slug. While flowing to the outlet of the channel, the slug is gradually condensed and shrank until being submerged in

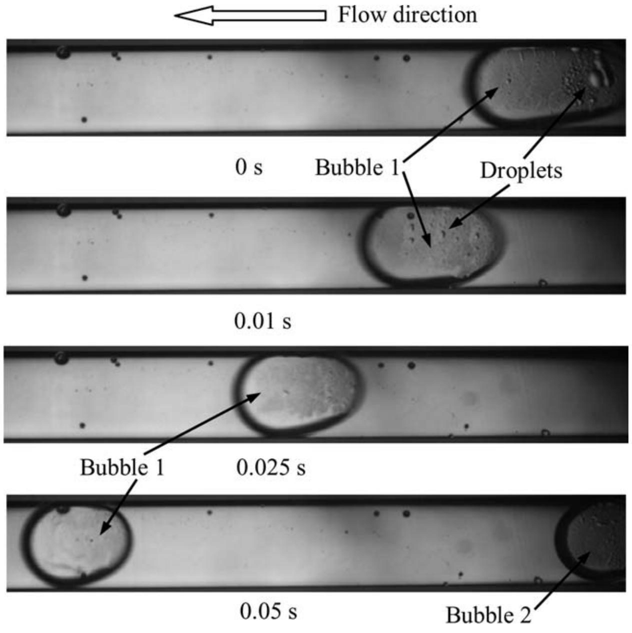

Figure 16. Droplet-slug/bubble compound flow ($Re_v = 918$, $Q = 56$ W, $X/L = 0.68$).

the condensate or flowing out the microchannel. At the downstream of the injection flow, the bubbles in the figures are observed, and at this position the channel is still mainly occupied by vapor. As shown in Figure 16, the droplets on the hydrophobic surface are observed inside Bubble 1 (see 0 s in Figure 16), indicating that the wide hydrophobic wall is not completely covered by the condensate. In this case, the bubbles shown in Figure 16 are actually cylinders. As the bubble flowing downstream, the length of bubble gets shorter owning to the condensation, and finally the channel surface is totally covered by condensate when no droplets inside the bubble (Bubble 1, 0.05 s in Figure 16).

It is important to note that the flow pattern of slug instability, reported by Fang et al.,[30] is quite different from the injection flow in this work. In their work, the vapor entrainment occurring at the transition point generates a queue of vapor plugs, which splits the liquid phase into segments, and the vapor slug coalesces with bubbles at microchannel corner during flowing downstream. In our experiment, by contrast, the vapor plugs shrink to bubbles or coalesce with other bubbles in the center of channels. The surface prepared by Fang et al.[30] is coated by a layer of self-assembled monolayers with contact angle of 123°, however, in current study, a thin Au film with thickness of 200 nm sputtered on the silicon wafer surface is utilized to obtain a hydrophobic surface with contact angle of 96°. In addition, the channel hydraulic diameter in current experiment (150 μm) is smaller than that of Fang's (285.7 μm).

Condensation heat transfer

Figure 17 presents the wall temperature distribution along the channel. As seen from the figure, the chip wall temperature increases with the increasing inlet vapor Reynolds number. Along the flow direction, the wall temperature decreases. Furthermore, before the injection, high-temperature vapor can directly contact with the channel wall and the wall temperature decrease mildly; however, after the injection flow, the microchannels are mainly occupied by condensate, resulting in distinct temperature drop on the wall after the injection flow.

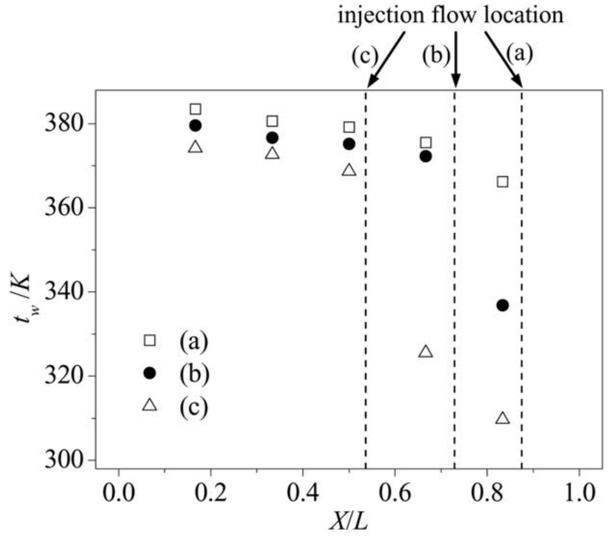

(a) Re_v=986, Q=59.5W, t_{in}=392.0K

(b) Re_v=916, Q=56.0W, t_{in}=384.9K

(c) Re_v=773, Q=48.01W, t_{in}=381.6K

Figure 17. Wall temperature distribution along the channel ($t_{\mathrm{cw,in}}$ = 289.8 K, G_w = 1.2 mL s^{-1}).

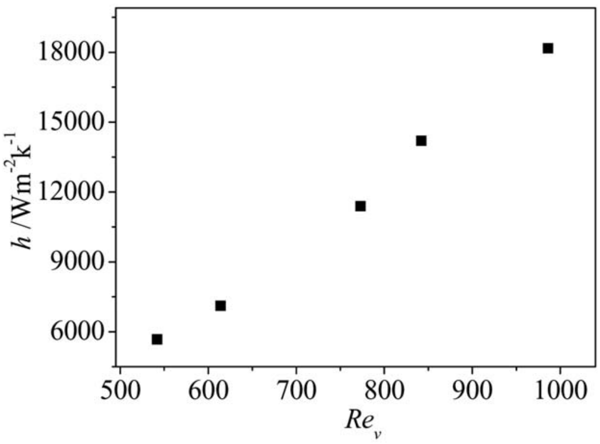

Figure 18. Average heat transfer coefficient ($t_{\mathrm{cw,in}}$ = 289.8 K, G_w = 1.2 mL s^{-1}).

Figure 18 describes the average heat transfer coefficient, h, as a function of inlet vapor Reynolds number. As shown in the figure, the average heat transfer coefficient increases with the increasing of inlet vapor Reynolds number, $\mathrm{Re_v}$. For a larger $\mathrm{Re_v}$, the injection flow is closer to channel outlet and hence enhance the heat transfer performance.

Conclusions

A visualization investigation has been conducted to investigate the flow condensation in hydrophobic, rectangular, silicon microchannels with hydraulic diameter of 150 μm. The hydrophobic surface has an equilibrium contact angle of 96°. Differing from the flow patterns in silicon microchannels without surface treatment, the droplet flow, droplet-annular compound flow, droplet-injection compound flow, and droplet-bubble/slug compound flow are observed in sequence along the flow direction in hydrophobic microchannels.

In droplet flow and droplet-annular compound flow region, the droplet grows in size and coalesces until reaching a critical size, and it detaches due to the steam drag force and sweeps other droplets on its way to the downstream. Three vapor slug/bubble breakup modes of droplet-injection compound flow, that is, long vapor ligament, short vapor ligament, and very short vapor ligament, are observed. With the increasing of inlet vapor Reynolds number and condensate Weber number, the location of droplet-injection compound flow is postponed, and the injection frequency is increased. In the droplet-slug/bubbly compound flow region, the previous and latter bubbles emitted from the injection flow may contact with each other and then bounce apart or merge into one bubble and flow to downstream rapidly. In particular, if the inlet vapor Reynolds number is large enough, injection tip may also impact and merge with previous generated bubble.

The chip wall temperature decreases mildly before the injection flow, after which there is a distinct temperature drop on the chip wall. In addition, for a larger inlet vapor

Reynolds number, the injection flow is closer to the channel outlet and hence the condensation heat transfer is enhanced.

Acknowledgments

The authors gratefully acknowledge the supports of the National Natural Science Foundation of China (51222605 and 11190015) and Natural Science Foundation of Jiangsu Province (BK20130009).

Notation

A = heat transfer area of single channel, m^2
A_c = cross-sectional area of single channel, m^2
c_p = specific heat of the cooling water, kJ kg^{-1} K^{-1}
d_{cri} = droplet critical size, m
D = hydraulic diameter of channel, m
f = exposure frequency, Hz
f_p = injection frequency, Hz
g = gravity, m s^{-2}
G_{cw} = volume flow rate of the cooling water, mL s^{-1}
h = heat transfer coefficient, W m^{-2} K^{-1}
m_l = condensation flow rate, kg s^{-1}
L = length of channel, m
M = number of injection period
n = number of channel
N = number of photograph
q = heat flux, W m^2
Q = heat flow rate, W
t_{in} = inlet saturated steam temperature, K
t_{out} = outlet condensation temperature, K
$t_{f,up}$ = the average temperature upstream the injection flow, K
$t_{f,down}$ = the average temperature downstream the injection flow, K
$t_{cw,in}$ = inlet temperature of the cooling water, K
$t_{cw,out}$ = outlet temperature of the cooling water, K
t_f = temperature of the condensation flow, K
t_w = temperature of the channel wall, K
Re_v = inlet vapor Reynolds number
We_l = condensation Weber number
X = distance between channel inlet and view point, m
X_p = distance between channel inlet and injection flow, m

Greek letters

η_s = dynamic viscosity of steam, kg m^{-1} s^{-1}
υ = viscosity, m^2 s^{-1}
ρ_v = density of vapour, kg m^{-3}
ρ_l = density of condensate, kg m^{-3}
ρ_{cw} = density of cooling water, kg m^{-3}
σ = surface tension, N m^{-1}

Literature Cited

1. Chen YP, Shi MH, Cheng P, Peterson GP. Condensation in microchannels. *Nanoscale Microscale Thermophys Eng.* 2006;12:117–143.
2. García-Cascales JR, Vera-García F, Gonzálvez-Maciá J, Corberán-Salvador JM, Johnson MW, Kohler GT. Compact heat exchanger modeling: condensation, *Int J Refrig-Rev Int Froid.* 2010;33:135–147.
3. Jang EY, Kang TJ, Im HW, Kim DW, Kim YH. Single-walled carbon-nanotube networks on large-area glass substrate by the dip-coating method. *Small.* 2008;4:2255–2261.
4. Médéric B, Miscevic M, Platel V, Lavieille P, Joly J. Experimental study of flow characteristics during condensation in narrow channels: the influence of the diameter channel on structure patterns. *Superlattices Microstruct.* 2004;35:573–586.
5. Garimella S. Condensation flow mechanisms in microchannels: basis for pressure drop and heat transfer models. *Heat Transfer Eng.* 2004;25:104–116.
6. Coleman JW, Garimella S. Characterization of two-phase flow patterns in small diameter round and rectangular tubes. *Int J Heat Mass Transfer.* 1999;42:2869–2881.
7. Agarwal A, Bandhauer TM, Garimella S. Measurement and modeling of condensation heat transfer in non-circular microchannels. *Int J Refrig-Rev Int Froid.* 2010;33:1169–1179.
8. Agarwal A, Garimella S. Representative results for condensation measurements at hydraulic diameter ~100 microns. *J Heat Transfer.* 2010;132:041010.
9. Bandhauer TM, Agarwal A, Garimella S. Measurement and modeling of condensation heat transfer coefficients in circular microchannels. *J Heat Transfer.* 2006;128:1050–1059.
10. Chen YP, Cheng P. Condensation of steam in silicon microchannels. *Int Commun Heat Mass Transfer.* 2005;32:175–183.
11. Wu JF, Shi MH, Chen YP, Li X. Visualization study of steam condensation in wide rectangular silicon microchannels. *Int J Therm Sci.* 2010;49:922–930.
12. Chen YP, Wu R, Shi MH, Wu JF, Peterson GP. Visualization study of steam condensation in triangular microchannels. *Int J Heat Mass Transfer.* 2009;52:5122–5129.
13. Wu HY, Cheng P. Condensation flow patterns in silicon microchannels. *Int J Heat Mass Transfer.* 2005;48:2186–2197.
14. Wu HY, Yu MM, Cheng P, Wu XY. Injection flow during steam condensation in silicon microshannels. *J Micromech Microeng.* 2007;17:1618–1627.
15. Quan XJ, Cheng P, Wu HY. An experimental investigation on pressure drops of steam condensing in silicon microchannels. *Int J Heat Mass Transfer.* 2008;51:5454–5458.
16. Quan XJ, Cheng P, Wu HY. Transition from annular flow to plug/slug flow in condensation of steam in microchannels. *Int J Heat Mass Transfer.* 2008;51:707–716.
17. Quan XJ, Cheng P, Dong LN, Cheng P. Determination of annular condensation heat transfer coefficient of steam in microchannel with trapezoidal cross sections. *Int J Heat Mass Transfer.* 2010;53:3670–3676.
18. Ma XH, Fan XG, Lan Z, Hao TT. Flow patterns and transition characteristics for steam condensation in silicon microchannels. *J Micromech Microeng.* 2011;21:075009.
19. Ma XH, Lan Z, Xu W, Wang M, Wang S. Effect of surface free energy difference on steam-ethanol mixture condensation heat transfer. *Int J Heat Mass Transfer.* 2012;55:531–537.
20. Zhang W, Xu JL, Thome JR. Periodic bubble emission and appearance of an ordered bubble sequence (train) during condensation in a single microchannel. *Int J Heat Mass Transfer.* 2008;51:3420–3433.
21. Zhang W, Xu JL. Flow pattern and multichannel effect of steam condensation in silicon microchannels. *J Eng Thermophys.* 2008;29;605–608.
22. Kuo CY, Pan C. Two-phase flow pressure drop and heat transfer during condensation in microchannels with uniform and converging cross-sections. *J Micromech Microeng.* 2010;20:095001.
23. Fang C, David M, Wang FM, Goodson KE. Influence of film thickness and cross-sectional geometry on hydrophilic microchannel condensation. *Int J Multiphase Flow.* 2010;36:608–619.
24. Zhao H, Beysens D. From droplet growth to film growth on a heterogeneous surface: condensation associated with a wettability gradient. *Langmiur.* 1995;11:627–634.
25. Leach RN, Stevens F, Langford SC. Dropwise condensation—experiments and simulations of nucleation and growth of water drops in a cooling system. *Langmiur.* 2006;22:8864–8872.
26. Wier KA, McCarthy TJ. Condensation on ultrahydrophobic surfaces and its effect on droplet mobility: ultrahydrophobic surfaces are not always water repellant. *Langmiur.* 2006;22:2433–2436.
27. Narhe RD, Beysens DA. Water condensation on a super-hydrophobic spike surface. *Europhys Lett.* 2006;75:98–104.
28. Dorrer C, Ruhe J. Condensation and wetting transitions on micro-structured ultrahydrophobic surfaces. *Langmiur.* 2007;23:3820–3824.
29. Anand S, Son SY. Sub-micrometer dropwise condensation under superheated and rarefied vapor condition. *Langmiur.* 2010;26:17100–17110.
30. Fang C, Steinbrenner JE, Wang FM, Goodson KE. Impact of wall hydrophobicity on condensation flow and heat transfer in silicon microchannels. *J Micromech Microeng.* 2010;20:045018.
31. Shang JY, Flury M, Harsh JB, Zollars RL. Comparison of different methods to measure contact angles of soil colloids. *J Colloid Interface Sci.* 2008;328:299–307.
32. Barajas AM, Panton RL. The effects of contact angle two-phase flow in capillary tubes. *Int J Multiphase Flow.* 1993;19:337–346.
33. Cheng P, Wu HY. Mesoscale and microscale phase change heat transfer. *Adv Heat Transfer.* 2006;39:461–563.
34. Li JM, Wang BX. Size effect on two-phase regime for condensation in micro/mini tubes. *Heat Transfer-Asian Res.* 2003;32(1):65–71.
35. Garimella S. Condensation flow mechanisms, pressure drop and heat transfer in microchannels. In: Kakaç S, Vasiliev LL, Bayazitoglu Y, Yener Y, editors. Microscale Heat Transfer: Fundamentals and Applications. The Netherlands: Springer, 2005:273–290.

36. Glassbrenner CJ, Slack GA. Thermal conductivity of Silicon and Germanium from 3°K to the melting point. *Phys Rev*. 1964;134: A1058–A1069.
37. Assael MJ, Antoniadis KD, Wu JT. New measurements of the thermal conductivity of PMMA, BK7, and Pyrex 7740 up to 450K. *Int J Thermophys.* 2008;29:1257–1266.
38. Goldman AJ, Cox RG, Brenner H. Slow viscous motion of a sphere parallel to a plane wall-I Motion through a quiescent fluid. *Chem Eng Sci*. 1967;22:637–651.
39. Goldman AJ, Cox RG, Brenner H. Slow viscous motion of a sphere parallel to a plane wall-II Couette flow. *Chem Eng Sci*. 1967;22: 652–660.
40. O'neill ME. A sphere in contact with a plane wall in slow linear shear flow. *Chem Eng Sci*. 1968;23:1293–1298.
41. Extran CW, Gent AN. Retention of liquid drops by solid surfaces. *J Colloid Interface Sci*. 1990;138:431–442.

Manuscript received Oct. 8, 2012, and revision received Oct. 12, 2013.